

Measurement of a topological edge invariant in a microwave network

Wenchao Hu,¹ Jason C. Pillay,² Kan Wu,³ Michael Pasek,² Perry Ping Shum,¹ and Y. D. Chong^{1,2,*}

¹*Centre for Disruptive Photonic Technologies, Nanyang Technological University, Singapore 637371, Singapore*

²*Division of Physics and Applied Physics, School of Physical and Mathematical Sciences, Nanyang Technological University, Singapore 637371, Singapore*

³*State Key Laboratory of Advanced Optical Communication Systems and Networks, Department of Electronic Engineering, Shanghai Jiao Tong University, Shanghai 200240, China*

We report on the measurement of topological invariants in an electromagnetic topological insulator analog formed by a microwave network, consisting of the winding numbers of scattering matrix eigenvalues. The experiment can be regarded as a variant of a topological pump, with non-zero winding implying the existence of topological edge states. In microwave networks, unlike most other systems exhibiting topological insulator physics, the winding can be directly observed. The effects of loss on the experimental results, and on the topological edge states, is discussed.

PACS numbers: 42.60.Da, 42.70.Qs, 73.43.-f

I. INTRODUCTION

Topological insulators are phases of matter that are “topologically distinct” from conventional insulators, meaning that their electronic bandstructures cannot be deformed into conventional bandstructures without closing bandgaps. They have many striking physical properties, the most notable being the existence of “topological edge states” which, in two dimensional (2D) topological insulators, have the unique property of being protected against backscattering from impurities. Topologically nontrivial bandstructures were originally discovered in condensed matter systems, first in the quantum Hall (QH) effect [1] and later in materials with strong spin-orbit coupling [2]. Recently, the concept has been extended to photonics, with coherent classical electromagnetic fields taking the place of electron wavefunctions [3–14]. Such “topological photonics” devices have been realized with microwave-scale magnetic photonic crystals [3–6] and meta-atom structures [7]; and, at optical and infrared frequencies, with waveguide lattices [8] and resonator lattices [9, 10]. There have also been theoretical proposals based on modulated photonic crystal resonances [11], circuit QED systems [12, 13], metamaterial photonic crystals [14], etc. The key feature of these devices is the existence of topologically protected electromagnetic edge states, which may have technological promise for waveguides that are robust against disorder. Topological photonics may also prove useful for studying aspects of topological insulator physics which are difficult or impossible to probe in the condensed-matter context, such as the effects of nonlinearity [15].

In condensed matter systems, the most important physical consequence of topologically nontrivial bandstructures is that they cause certain macroscopic transport properties to be precisely quantized. Most famously, in the integer QH effect, the Hall conductance is quan-

tized to integer multiples of the inverse von Klitzing constant to nearly one part in 10^9 [16]. An influential explanation for this was supplied by Thouless *et al.* [17], who showed using linear response theory that the QH conductance is tied to the Chern numbers of the bands, which are “topological invariants” restricted to integer values. In photonics, however, there is no direct analog of the Hall conductance or similar linear response-based quantity, due to the absence of a fermionic ground state [3, 4]; this is why edge propagation measurements have served almost exclusively as the signature for topologically nontrivial photonic bandstructures.

In this paper, we present experimental measurements of a topological edge invariant in a microwave network. The invariant consists of the integer winding numbers of scattering matrix (S matrix) eigenvalues, measured at the edges of the sample. The experiment is a variant of the “topological pump”, a thought experiment invented by Laughlin to explain the QH effect in topological terms—in a way that does *not* rely on linear response [18, 19]. In Laughlin’s original setup, the Hall conductance is described in terms of the adiabatic “pumping” of single-electron wavefunctions across the surface of a cylinder; due to the cylindrical geometry, the pumping can be expressed as the effect of a gauge transformation, whereupon the robustness of the QH effect follows as a result of the exactness of gauge invariance. The topological pump can also be formulated in terms of scattering processes [20–22], which is a particularly natural approach for describing electromagnetic systems [23]. As described below, the present experiment is based on this scattering formulation. It is remarkable that, even though the topological pump is typically regarded as a “thought experiment”, it can actually be implemented in electromagnetic systems. Recently, topological pumps have been demonstrated in 1D quasicrystalline arrays of optical waveguides [24, 25], and a related scheme based on a ring of coupled optical resonators has been proposed by Hafezi [26]. Compared to these previous works, our microwave experiment is noteworthy in that the measurements are not limited to intensities, but include full phase infor-

* yidong@ntu.edu.sg

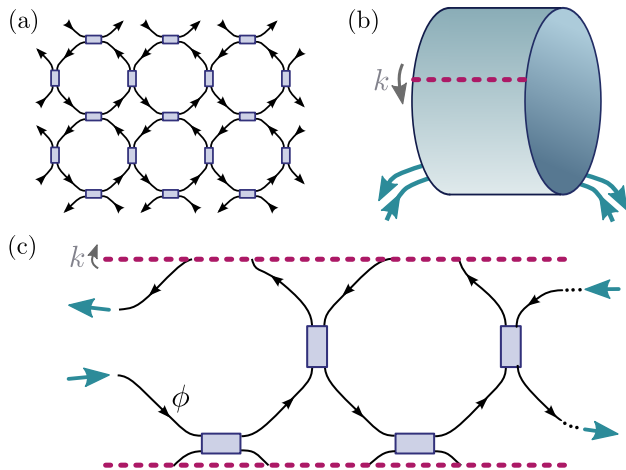


FIG. 1. (a) Schematic of a periodic 2D directed network. Wave amplitudes undergo phase delay ϕ along each directed link (black arrows), and couple through a 2×2 unitary matrix at each node (blue boxes). (b) In a “topological pump” setup, a 2D system is rolled into a cylinder; twisted boundary conditions with tunable twist angle k are applied, and a transport measurement is performed in the axial direction (cyan arrows). (c) Topological pump setup for a network model, with a cylinder comprising one unit cell in the azimuthal direction and two cells in the axial direction.

mation, since the complex S matrix can be determined with a microwave network analyzer; this allows the winding process to be directly observed. The difference between topologically trivial and nontrivial behaviors is also clearly observable in this system. The setup also provides a platform for studying the topological properties of “Floquet” or “quasi-energy” bandstructures, a topic of current theoretical interest [27–33].

The remainder of this paper is organized as follows: Section II reviews the theory of network bandstructures and topological pumps; Section III describes the experimental setup and results; finally, Section IV discusses the implications of the experiment, including how we can understand the effects of losses on the topological edge invariant and the network bandstructure.

II. BANDSTRUCTURES AND TOPOLOGICAL PUMPS IN NETWORKS

A. Network bandstructures

Our realization of an electromagnetic topological insulator is a network implemented with microwave components. Such a system is best understood using the framework of a “network model” [34], which differs in several respects from the tight-binding Hamiltonian models familiar to most readers. This section describes our network model and its topological properties. A more detailed discussion may be found in Ref. [23].

Network models, which originated in the QH litera-

ture as a convenient way to study disordered QH systems [34] and other types of topological insulators [35, 36], describe directed networks within which waves can propagate. We consider the specific periodic (disorder-free) network shown in Fig. 1(a), which consists of unit cells arranged in a 2D square lattice, each cell containing two nodes and four directed links. A “solution” to the network is a set of wave amplitudes (complex scalars) defined along the links, such that (i) traversing each link incurs a phase delay ϕ (which we take to be the same for all links), and (ii) the amplitudes entering and leaving each node are related by a fixed 2×2 coupling matrix. Let the complex vector $|\psi\rangle$ be the collective set of wave amplitudes exiting the links, and $|\psi'\rangle = e^{-i\phi}|\psi\rangle$ be the amplitudes entering the links. The individual node coupling matrices can be composed into a matrix U that relates the amplitudes entering and leaving the nodes. These amplitudes must be equal to $|\psi\rangle$ and $|\psi'\rangle$ respectively, so

$$U|\psi\rangle = e^{-i\phi}|\psi\rangle. \quad (1)$$

For an infinite periodic network, we look for solutions obeying Bloch’s theorem. Then Eq. (1) reduces to [23, 37]

$$U_k|\psi_{nk}\rangle = e^{-i\phi_n(k)}|\psi_{nk}\rangle, \quad (2)$$

where n is the band index, k is the quasimomentum, and $\phi_n(k)$ is the band “quasi-energy”. In the absence of gain or loss in the network, U_k is unitary, and $\phi_n(k)$ is real. But unlike a usual band energy, it is an angle variable.

Interestingly, Eq. (2) has the same form as the evolution equation for a lattice with a time-periodic Hamiltonian, where U_k is the evolution operator over one period and $|\psi_{nk}\rangle$ is a Floquet state of the driven lattice. Recently, several groups have proposed a new class of topological insulators called “Floquet topological insulators”, where the topological behavior arises from periodic drives (such as oscillating electric fields). It has been shown that a driven system can have a topologically nontrivial *quasi-energy* bandstructure, even if the undriven *energy* bandstructure is topologically trivial [27–33].

The network model framework is also useful for describing a type of photonic device proposed and realized by Hafezi *et al.*, consisting of a lattice of ring resonators joined by auxiliary waveguides [9, 10]. By engineering incommensurate modulations into the auxiliary waveguides, those authors induced an effective tight-binding “vector potential” corresponding to a uniform magnetic field. The system thus maps onto a QH system, and exhibits electromagnetic analogs of QH edge states [10]. Surprisingly, however, even if the auxiliary waveguides are symmetrical and commensurate, corresponding to zero “magnetic flux”, full-wave simulations show that robust one-way edge states can still exist [38]. This is explained by moving beyond the tight-binding description, and formulating a network model where the arms of the ring resonators are links [23, 37, 38]. That network model is equivalent to the one considered in this paper.

In most respects, quasi-energy bandstructures have the same behaviors as energy bandstructures. If quasi-energy

bands have nonzero Chern numbers (as calculated from $|\psi_{nk}\rangle$ in the usual way [17]), topological edge states will exist; this is the case demonstrated in a recent photonic realization of a Floquet topological insulator [8]. However, a quasi-energy bandstructure can also be topologically nontrivial *even if all Chern numbers are zero* [30]. This case, which we call the “anomalous Floquet insulator”, is possible because $\phi_n(k)$ is an angle variable; for example, every band can receive +1 to its Chern number from the band above and -1 from the band below, resulting in zero net Chern number even though all bandgaps are topologically nontrivial. For driven systems, Rudner *et al.* have proposed an alternative topological bulk invariant which can characterize this situation [33]. The topological nontriviality of an anomalous Floquet insulator can also be verified from the presence of topological edge states, and from its behavior under topological pumping (as described in the next section) [23].

For the periodic network of Fig. 1, the quasi-energy bandstructure can be obtained analytically [37]. It turns out that the band topology depends on a single parameter $\theta \in [0, \pi/2]$, which describes the coupling strength at the network nodes. The bandgaps close at $\theta = \pi/4$. For $\theta < \pi/4$, the system is a topologically trivial conventional insulator; when $\theta > \pi/4$, the system is an anomalous Floquet insulator [23]. In the experiment, this allows us to switch easily between topologically trivial and nontrivial behaviors.

B. Topological pumps

A topological pump is an experiment which is specially designed to reveal the topological properties of a 2D lattice. As shown schematically in Fig. 1(b), it consists of rolling a 2D lattice into a cylinder, inducing a phase “twist” k in the azimuthal boundary conditions, and performing a transport measurement in the axial direction (i.e., at the edges of the cylinder). In the original Laughlin thought experiment [18], the twist is implemented by adiabatically threading magnetic flux through the cylinder, which produces an Aharonov-Bohm phase shift while also transporting electron wavefunctions in the axial direction. Threading one magnetic flux quantum induces a 2π phase shift; by gauge invariance, the number of transported electrons must be an integer. From this, the quantization of the Hall conductance can be derived [18].

An alternative formulation of the topological pump, based on wave scattering, has been developed by Brouwer and co-workers [20, 21]. Here, one imagines taking a similar cylinder, and scattering electron waves (or electromagnetic waves, as the case may be) off one edge, at an energy (or frequency) which lies in a bulk bandgap. As the twist angle k advances by 2π , the reflection matrix r is measured. For a sufficiently long cylinder and/or a sufficiently large bandgap, transmission to the opposite edge is negligible and r is unitary; its eigenvalues lie on the unit circle, and their trajectories during a pumping cycle

can be topologically characterized by a winding number. A nonzero winding number corresponds to a topologically nontrivial sample. This is tied to the existence of topological edge states. In a topologically nontrivial system, edge states must occur at certain values of k during the pumping cycle [19]. According to scattering theory, each such occurrence induces a π scattering phase shift [21]. Such a phase shift can only be guaranteed if the eigenvalue trajectories have nonzero winding. This behavior is “topologically protected”, since weak perturbations deform the trajectories of the reflection eigenvalues without altering the winding number, and the only way to remove the winding is to close the band gap.

Our experiment implements a similar scheme, in the context of a microwave network, as shown in Fig. 1(c). The tunable twist k is implemented by connecting the links (microwave cables) at each end of the “azimuthal axis” to phase shifters. We measure the full scattering parameters along the axis (i.e., the complex reflection and transmission coefficients for microwave signals injected into the edges of the cylinder), thus obtaining the S matrix, which is 2×2 for this network geometry. In the ideal situation where the network is completely lossless, S is unitary, and its eigenvalues σ_{\pm} lie on the unit circle. If the quasi-energy ϕ lies in a sufficiently large bandgap, then the transmission goes to zero, and σ_{\pm} reduce to the reflection coefficients from each edge (this condition can indeed be met, as discussed in Section IV). The winding numbers of σ_{\pm} , as the twist angle k is tuned through 2π , are the desired integer invariants [20–23].

Several other schemes to directly measure topological invariants have recently appeared in the literature. Most prominently, a topological pump has been realized experimentally using a 1D quasicrystalline optical waveguide array, which can be mapped formally to a 2D QH system [24, 25]. A scheme to implement a topological pump in a 2D system has recently been proposed by Hafezi [26]. Here, coupled resonators are arranged in an annulus, with a tunable phase shift along one column of the annulus; such a configuration is similar to the Laughlin thought experiment [18], and to the present experiment. A topological invariant is then inferred from the transport of resonance peaks in the transmission spectrum along the edge. This proposal has yet to be realized.

Topological pumps, such as the present experiment and the related schemes described in the preceding paragraph, are probes of topological *edge* invariants. There have also been theoretical proposals to directly measure topological *bulk* invariants—specifically, Chern numbers—in photonic systems [39, 40]. Typically, a bulk invariant is significantly more challenging to measure than an edge invariant, as it requires detailed information about the wavefunctions in the bulk, whereas the latter depends only on the response of the system at a single frequency or quasi-energy [21]. Furthermore, as noted above, edge invariants can detect topologically nontrivial behaviors in cases where the band topology cannot be fully characterized by Chern numbers [23]. (A recent

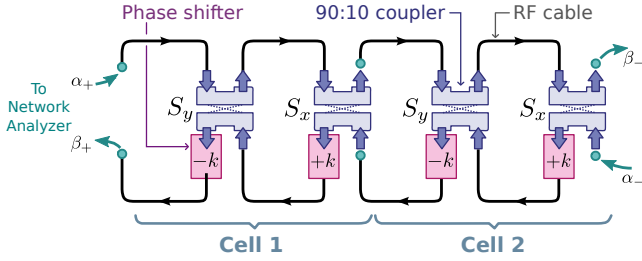


FIG. 2. Experimental setup. Each of the identical units, labeled here “Cell 1” and “Cell 2”, corresponds to one cell in the topological pump geometry of Fig. 1. A pair of phase shifters in each cell (pink boxes), with shifts of $+k$ and $-k$ respectively, implement the twisted boundary condition. The couplers (blue rods) are depicted in the “strong coupling” configuration; the “weak coupling” configuration is achieved by swapping each coupler’s outputs. The overall input and output amplitudes are α_{\pm} and β_{\pm} ; their scattering parameters are measured with a network analyzer.

experiment has measured a topological bulk invariant in a specific 1D system [41].)

III. EXPERIMENTAL SETUP AND RESULTS

Our experimental setup is shown in Fig. 2. The network is divided into identical subunits, each consisting of 4 cables, 2 phase shifters, and 2 couplers. By comparison with Fig. 1(c), each subunit is equivalent to a “cylinder” in the topological pump setup that is one cell wide and one cell long. Connecting the subunits in series forms a longer cylinder; Fig. 2 shows a “two-cell” configuration. The cables are standard low-loss coaxial RF cables of ~ 15 cm length, and the couplers are four-port single-directional couplers, with isolators built into each port and coupling ratios of approximately 90:10 (DTO-2.5/5-10, Shanghai Huaxiang Computer Ltd.). The two phase shifters in each cell (TKE-90-6SA, Shanghai Huaxiang Computer Ltd.) are independently tunable, and set to produce $+k$ and $-k$ phase shifts respectively. The operating frequency is chosen to be 5 GHz, low enough to reduce losses in the various components while high enough to allow phase shifts in the full range $k \in [0, 2\pi]$. There is one input port and one output port at each end of the network, connected to a vector network analyzer (Anritsu 37396C). From this, we measure the S matrix, defined as

$$S \begin{bmatrix} \alpha_+ \\ \alpha_- \end{bmatrix} = \begin{bmatrix} \beta_+ \\ \beta_- \end{bmatrix}, \quad (3)$$

where $\{\alpha_{\pm}, \beta_{\pm}\}$ are the input and output wave amplitudes at the two edges, as labeled in Fig. 2.

Since the couplers have fixed coupling ratios, we are unable to continuously vary the network’s coupling strength parameter, on which the bandstructure topology depends. However, by swapping the order of each

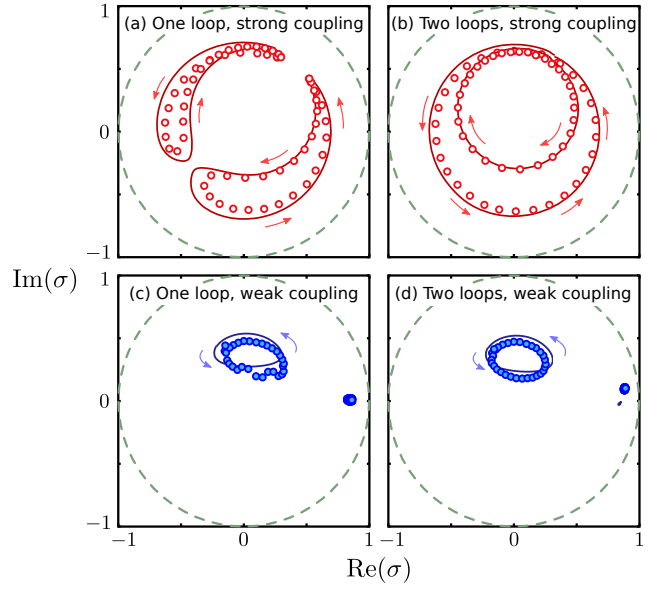


FIG. 3. Scattering matrix eigenvalues measured across one cell (left) and across two cells in series (right). Arrows indicate the direction of motion with increasing k . Circles show experimental data; solid curves show theoretical calculations using the scattering parameters measured for each network component individually (including losses). Non-zero winding numbers can be observed in the strong-coupling two-cell case. The unit circle is indicated by dashed curves.

coupler’s output ports, we can switch between the two cases of a topologically trivial and nontrivial bandstructure. As described in Section II A and Ref. 37, the strength of each coupler is described by a parameter $\theta \in [0, \pi/2]$, where $\theta = 0$ corresponds to zero coupling between adjacent unit cells and $\pi/2$ is complete coupling. The bandstructure is topologically trivial for $\theta < \pi/4$, and nontrivial for $\theta > \pi/4$, independent of all other coupling matrix parameters. Our 90:10 couplers thus allow for either $\theta \approx \tan^{-1}(3) \approx 0.40\pi$ (topologically nontrivial; this is the configuration shown in Fig. 2) or $\theta \approx \tan^{-1}(1/3) \approx 0.10\pi$ (topologically trivial). At the 5 GHz operating frequency, each cable has phase delay $\approx 0.2\pi$, which lies in a bandgap of the quasi-energy bandstructure for both the strong and weak-coupling cases. The loss in each cable is ≈ 0.4 dB.

The measured S matrix eigenvalues are shown in Fig. 3. The eigenvalues do not lie on the unit circle, due to losses in the network which make the S matrix sub-unitary. Nonetheless, the eigenvalue trajectories exhibit winding behaviors very similar to the lossless case. For the one-cell system under strong coupling, the two S matrix eigenvalues, σ_{\pm} , move along distinct closed trajectories as k is increased through 2π , as shown in Fig. 3(a). Each individual trajectory does not encircle the origin (i.e. the winding number is zero), even though the network bandstructure is in the topologically nontrivial regime. This is because topological protection requires the opposite edges in a finite system to be well

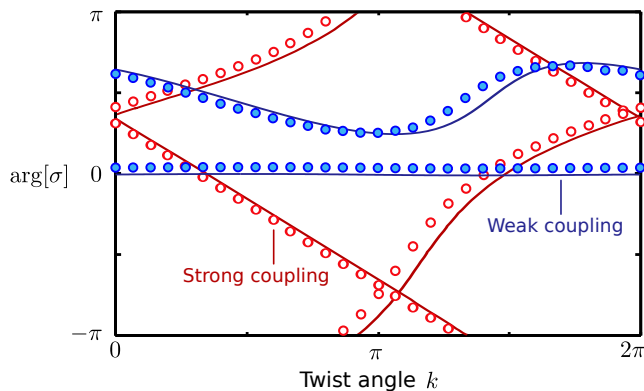


FIG. 4. Arguments of the complex S matrix eigenvalues for the two-cell network, as the phase shift k is tuned through 2π . Empty circles show the strong coupling measurement data, and filled circles show the weak coupling data; solid curves show theoretical calculations. For strong coupling, the two eigenvalues have winding numbers ± 1 , corresponding to the bulk bandstructure being topologically nontrivial.

separated, so as to have negligible overlap between the counter-propagating edge states on each edge. When the separation is increased by connecting two cells in series, the trajectories coalesce into a pair of loops with winding numbers ± 1 , as shown in Fig. 3(b). By contrast, in the weak coupling regime of Figs. 3(c) and 3(d), the eigenvalues move along separate trajectories without encircling the origin.

The winding numbers can also be visualized by plotting $\arg[\sigma_{\pm}]$ against k , as in Fig. 4. It is worth noting that, in the topologically nontrivial regime, the two S matrix eigenvalues wind in opposite directions. This corresponds to the fact that the topological edge states on opposite edges have opposite group velocities. In terms of the projected bandstructure, one branch of edge state have a dispersion curve that crosses the probed value of ϕ from above, and the other from below; hence, the induced scattering phase shifts have opposite signs.

IV. DISCUSSION

Our experiment deviates from an ideal topological pump in several respects. Firstly, as previously mentioned, in the ideal topological pump the edges are separated by a large number of unit cells, so that there is a true “bulk”, whereas in our experiment there are only two unit cells. However, this does not make a significant difference to the physical interpretation, as the relevant phenomenon—the emergence of a non-zero winding number—is observed already when going from the one-cell to the two-cell case, shown in Figs. 3(a) and (b). This arises from the fact that the system is deep in either the topologically trivial or nontrivial phases, based on our choices of the coupling strength θ ; in the nontrivial case, each edge state is strongly confined to one unit cell, with

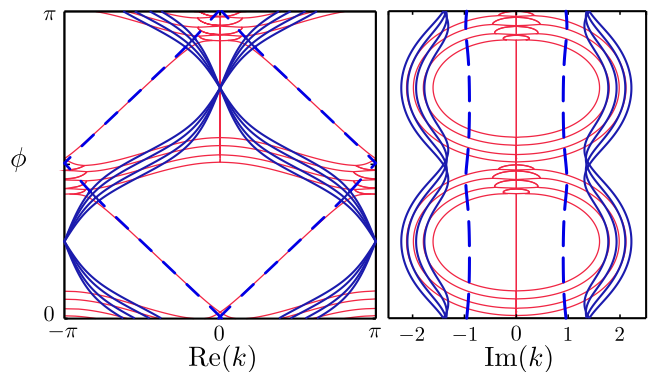


FIG. 5. Complex projected bandstructure of a hypothetical lossy network (blue lines), consisting of an infinite strip 5 unit cells wide. Each link has real tunable phase delay ϕ , each coupler has loss $e^{-\gamma}$ in each output port where $\gamma = 0.25$, and each edge of the strip obeys lossy boundary conditions $r_{\pm} = \exp(-0.2\pi)$, chosen to be roughly the same as in the experiment. The coupling strength is $\theta = 0.4\pi$, approximately equal to the “strong coupling” (topologically nontrivial) configuration in the experiment. The bandstructure for the lossless network ($\gamma = 0$ and $|r_{\pm}| = 1$) is plotted for comparison (red lines). The lossy network exhibits edge states whose dispersion relations are almost identical to the lossless network’s topological edge states, and have lower loss than all other states (blue dashes).

negligible amplitude on the next unit cell. Indeed, calculations based on realistic parameters show no significant changes in the trajectory of the S matrix eigenvalues as the number of cells is increased beyond two.

When the edges are well-separated, the S matrix reduces to a pair of reflection coefficients $r_{\pm} \equiv \beta_{\pm}/\alpha_{\pm}$, where $\{\alpha_{\pm}, \beta_{\pm}\}$ are the input/output wave amplitudes labeled in Fig. 2. This is observed in the small transmission coefficients in the two unit cell systems: $|t| < 0.06$ in the strong coupling system and $|t| < 0.04$ in the weak coupling case. Simulations of a larger system (with 5 unit cells) reveal that the edge states have penetration depths of less than half a unit cell, as determined by the exponential decay of the wave intensity (see Appendix A).

Another difference between our experiment and the ideal topological pump is the presence of loss in all the network components: the cables, phase shifters, and couplers. As a result, the eigenvalues of the S matrix are not strictly constrained to the unit circle, as seen in Fig. 3. Nonetheless, we argue that these eigenvalue trajectories can be meaningfully linked to the existence or non-existence of topological edge states, based on the close relationship between the edge scattering parameters measured in the experiment and the projected bandstructure of the network.

In the experiment, r_{\pm} is determined based on two parameters ϕ and k , with all other parameters (such as the coupling matrices) fixed; varying k then gives results like those shown in Fig. 3 and Fig. 4. Alternatively, we could

either (i) determine ϕ given r_{\pm} and k (by finding the eigenvalues of the scattering matrix for one period of an infinite strip [23]), or (ii) determine k given r_{\pm} and ϕ (by finding the eigenvalues of the transfer matrix for one period of the strip). Both procedures yield the projected bandstructure, with r_{\pm} interpreted not as reflection coefficients, but as *boundary conditions* which are applied along the edge of the strip, specifying the phase shifts on the edge links. In the absence of losses, if the scattering experiment yields a non-zero winding number for ϕ in a bulk bandgap, then it can be seen that the projected bandstructure exhibits topological edge states [23].

Now, consider a lossy network. The losses can be described, without loss of generality, by making the coupling matrices sub-unitary, as well as by setting $|r_{\pm}| < 1$ (lossy boundary conditions). The two procedures described in the preceding paragraph, (i) and (ii), lead to two distinct types of complex projected bandstructure; we focus on procedure (ii), which takes r_{\pm} and a real ϕ and yields complex wave-numbers k , whose imaginary parts are the attenuation constants of the propagating modes. One such complex bandstructure is shown in Fig. 5, generated using representative lossy r_{\pm} and coupling matrices (a 5-cell-wide strip is used for clarity). The bandstructure contains clearly-defined edge states whose dispersion curves have real parts nearly indistinguishable from the lossless network's topological edge states. Apart from these, there also exist propagating bulk states. Even in the range of ϕ corresponding to the lossless network's bulk bandgap, there are bulk states with $\text{Re}[k] \neq 0$, which are continuable to purely evanescent ($\text{Re}[k] = 0$) states of the lossless system. However, these bulk states have significantly larger attenuation $|\text{Im}(k)|$ compared to the edge states, which can be attributed to the fact that they experience losses over a wider area. If we wind $\arg[r_{\pm}]$ through 2π , with fixed $|r_{\pm}| < 1$ (corresponding to a sub-unitary trajectory in the complex plane), the part of the complex projected bandstructure corresponding to the bulk states remains nearly unchanged, in both its real and imaginary parts. For the edge states, the real part of the dispersion curve winds with $\arg[r_{\pm}]$, whereas the imaginary part remains nearly unchanged. Hence, winding $\arg[r_{\pm}]$ has the effect of “pumping” a branch of lossy edge states across one quasi-energy period.

In summary, we have observed a topological edge invariant, based on topological pumping, in a classical microwave network. Since networks of this sort are rather simple to set up, this may be a convenient method for studying the physics of topological bandstructures. For instance, we have discussed how the quasi-energy bandstructures which arise in networks can have the same properties as the bandstructures of Floquet topological insulators [27–32]. In the square-lattice network chosen for the present experiment, the topologically nontrivial phase is an “anomalous Floquet insulator”, which possesses topological edge states despite all bands having zero Chern number [29]. In other network geometries, such as hexagonal lattices, different parameter choices

give rise to either anomalous Floquet insulator phases, Chern insulator phases (in which the Chern numbers are nonzero), or conventional insulator phases [23]. If couplers with tunable coupling strengths are implemented, the transitions between these various phases could be directly observed. In future work, it would be desirable to reduce the losses in the network components, though it is encouraging that a non-zero winding is already clearly observable even at the current loss levels. Based on our above arguments, the edge states are physically meaningful despite the presence of loss; although both edge states and bulk states undergo attenuation, the two types of state are clearly distinguishable in the complex projected bandstructure. Since the edge states receive significantly less attenuation, they are the dominant mode of transmission along the edge.

V. ACKNOWLEDGMENTS

We are grateful to M. Hafezi, M. Rechtsman, B. Zhang, C. Soci, and N. Zheludev for helpful discussions. This research was supported by the Singapore National Research Foundation under grant No. NRFF2012-02, and by the Singapore MOE Academic Research Fund Tier 3 grant MOE2011-T3-1-005.

Appendix A: Scattering and transfer matrices

Fig. 6 shows one cell of the network in our pumping experiment. In terms of the cylindrical geometry of the topological pumping experiment (as depicted in Fig. 1 of the main text), the horizontal direction in this figure corresponds to the cylinder axis, and the vertical direction corresponds to the cylinder's azimuthal direction. The inputs to the cell are the complex wave amplitudes $\{d, b'\}$, and the outputs are $\{b, d'\}$. We can increase the separation between the left and right edges of the network by “stacking” identical cells along the horizontal (axial) direction.

We first consider the lossless case. Within each cell, the wave amplitudes are multiplied by $\exp(i\phi)$ when crossing each link. At the couplers, the wave amplitudes are related by

$$S_y \begin{bmatrix} d e^{i\phi} \\ c e^{i(\phi+k)} \end{bmatrix} = \begin{bmatrix} b e^{-i(\phi-k)} \\ a e^{-i\phi} \end{bmatrix}, \quad (\text{A1})$$

$$S_x \begin{bmatrix} a \\ b' \end{bmatrix} = \begin{bmatrix} d' \\ c \end{bmatrix}, \quad (\text{A2})$$

where $S_{x,y}$ are 2×2 unitary matrices. We can combine (A1)–(A2) to eliminate a and c ; this results in a transfer matrix equation of the form

$$M(\phi, k) \begin{bmatrix} d \\ b \end{bmatrix} = \begin{bmatrix} d' \\ b' \end{bmatrix}, \quad (\text{A3})$$

where

$$M(\phi, k) \equiv \frac{1}{S_x^{22} S_y^{12}} \begin{bmatrix} -\det(S_x) \det(S_y) e^{2i\phi} - S_x^{12} S_y^{11} e^{-ik} & \det(S_x) S_y^{22} e^{ik} + S_x^{12} e^{-2i\phi} \\ S_x^{21} \det(S_y) e^{2i\phi} - S_y^{11} e^{-ik} & -S_x^{21} S_y^{22} e^{ik} + e^{-2i\phi} \end{bmatrix}. \quad (\text{A4})$$

The transfer matrix across one cell satisfies $\det(M) = S_x^{11} S_y^{21} / S_x^{22} S_y^{12}$; in this sense, it is generally not a “reciprocal” transfer matrix, unlike the transfer matrices encountered in wave propagation problems. That is to be expected, since the network’s input and output ports are inequivalent, and the links in the network are directional.

Several different quantities can be computed from Eqs. (A3)–(A4). Firstly, if the stack is infinite in extent, we can look for Bloch solutions satisfying

$$d' = e^{ik_x} d, \quad b' = e^{ik_x} b. \quad (\text{A5})$$

Hence, the eigenvalues of $M(\phi, k)$ are values for $\exp(ik_x)$, where k_x is the quasimomentum in the \hat{x} direction, for given values of quasi-energy ϕ and \hat{y} -quasimomentum k . This is essentially the calculation for the bulk quasi-energy bandstructure. The solution can be obtained analytically [37], by using the convenient parameterization

$$S_\mu = \begin{bmatrix} \sin(\theta_\mu) e^{i\chi_\mu} & -\cos(\theta_\mu) e^{i(\varphi_\mu - \xi_\mu)} \\ \cos(\theta_\mu) e^{i\xi_\mu} & \sin(\theta_\mu) e^{i(\varphi_\mu - \chi_\mu)} \end{bmatrix}, \quad \mu = x, y. \quad (\text{A6})$$

The angle θ_μ describes the “coupling strength”, with $\theta = 0$ corresponding to zero coupling between adjacent cells. One can show, after tedious calculation, that the quasi-energy bandstructure is gapless for $\theta_x + \theta_y = \pi/2$ [37]. This defines two distinct insulator phases: a weak-coupling insulator ($\theta_x + \theta_y < \pi/2$) and a strong-coupling insulator ($\theta_x + \theta_y > \pi/2$). These will turn out to be topologically distinct as well.

We now stack n cells together to form a one-dimensional lattice. Let $\{d_L, b_L, d_R, b_R\}$ be the input/output amplitudes on the left and right edges of the stack. Then

$$M_n(\phi, k) \begin{bmatrix} d_L \\ b_L \end{bmatrix} = \begin{bmatrix} d_R \\ b_R \end{bmatrix}, \quad \text{where } M_n \equiv [M(\phi, k)]^n. \quad (\text{A7})$$

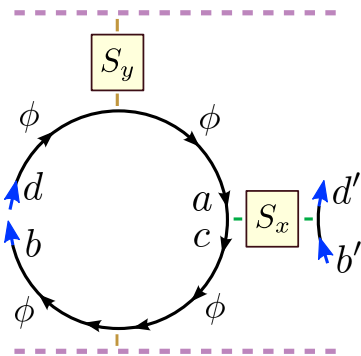


FIG. 6. Schematic of one cell of the network. The variables a , b , c , d , d' , and b' label the complex wave amplitudes at the indicated points along the links (cables). The boxes labeled S_x and S_y are 2×2 directional couplers. The horizontal dashed lines indicate boundaries related by a twisted boundary condition with twist angle k .

This can be rearranged into a scattering matrix equation,

$$S_n(\phi, k) \begin{bmatrix} d_L \\ b_R \end{bmatrix} = \begin{bmatrix} b_L \\ d_R \end{bmatrix}, \quad (\text{A8})$$

where

$$S_n \equiv \frac{1}{M_n^{22}} \begin{bmatrix} -M_n^{21} & 1 \\ \det(M_n) & M_n^{12} \end{bmatrix}. \quad (\text{A9})$$

Without losses, $S_n(\phi, k)$ is unitary and its two eigenvalues are unimodular. The diagonal entries of S_n are the left and right reflection coefficients, and the off-diagonal entries are the transmission coefficients.

We are interested in the variation of the eigenvalues of S_n with k , and specifically their winding numbers. If ϕ is chosen to be in the bulk bandgap, then for large n (i.e., a long cylinder), the transmission coefficients go to zero and S_n reduces to a diagonal matrix. Then the two eigenvalues are simply the two reflection coefficients, and are predicted to have winding number 0 in the weak-coupling insulator phase, and winding numbers ± 1 in the strong-coupling insulator phase. The numerical results agree, as shown in Fig. 7. This winding behavior can be deduced from the principle that bound states induce π phase shifts in the reflection coefficient [21], or by considering how edge state branches are transported across the bandgap in the projected quasi-energy bandstructure [23].

It is instructive to see how this works in the limits of very weak or very strong coupling. Firstly, for $\theta_x = \theta_y = 0$, the reflection coefficients are k -independent:

$$\frac{b_L}{d_L} = -e^{i(4\phi + \xi_x + \varphi_y)}, \quad \frac{d_R}{b_R} = -e^{i(\varphi_x - \xi_x)}. \quad (\text{A10})$$

And for $\theta_x = \theta_y = \pi/2$,

$$\frac{b_L}{d_L} = e^{i(2\phi + \chi_y)} e^{-ik}, \quad \frac{d_R}{b_R} = e^{i(2\phi + \varphi_x + \varphi_y - \chi_y)} e^{ik}, \quad (\text{A11})$$

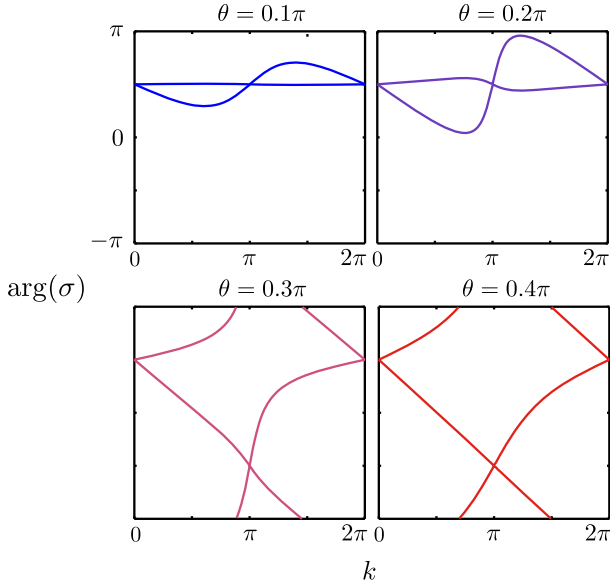


FIG. 7. Complex argument of the S_n matrix eigenvalues, σ , for lossless networks with $n = 10$ cells. Four different values of the coupling strength θ are shown. The S_x and S_y coupling matrices are taken to be equal and lossless with $\varphi = \chi = 0$ and $\xi = \pi/2$. The quasi-energy is $\phi = 0.25\pi$ (mid-gap). The system is topologically trivial for $\theta < \pi/4$, and non-trivial for $\theta > \pi/4$.

which results in winding numbers of ± 1 . For these two limiting cases, the bulk bands are completely flat. For intermediate values of θ , however, it is necessary to choose a value of ϕ that lies in the bulk bandgap, for the topological pumping procedure to make sense.

Appendix B: Losses

Losses can be incorporated into the model by multiplying each entry of the coupling matrices, S_x and S_y , by damping factors. This makes the coupling matrices sub-unitary:

$$S_\mu = \begin{bmatrix} \sin(\theta_\mu) e^{i\chi_\mu} e^{-\gamma_\mu^{11}} & -\cos(\theta_\mu) e^{i(\varphi_\mu - \xi_\mu)} e^{-\gamma_\mu^{12}} \\ \cos(\theta_\mu) e^{i\xi_\mu} e^{-\gamma_\mu^{21}} & \sin(\theta_\mu) e^{i(\varphi_\mu - \chi_\mu)} e^{-\gamma_\mu^{22}} \end{bmatrix}, \quad (\text{B1})$$

where $\mu = x, y$. In principle, each of the $\exp(-\gamma_\mu^{ij})$ factors can be independent. Losses occurring within the cables (links) or phase shifters can be incorporated into these coupling matrix damping factors, without loss of generality.

When losses are present, the S_n matrix defined in Eq. (A8) becomes sub-unitary, i.e. its eigenvalues lie inside the unit circle. Hence, in the large- n limit the reflection coefficients have magnitudes smaller than unity, reflecting the fact that the input waves undergo dissipation within the network.

Fig. 8 shows the trajectories of the eigenvalues of S_n

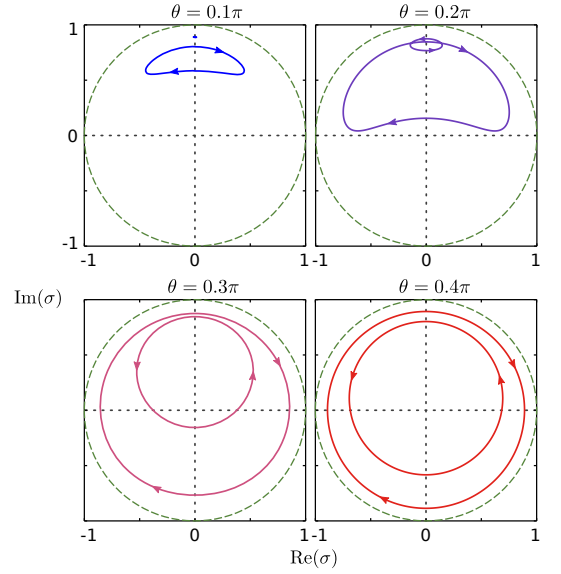


FIG. 8. Trajectories of the S_n matrix eigenvalues in the complex plane, as k advances from 0 to 2π . The network parameters are the same as in Fig. 7, except that loss is present: each coupling matrix S_x and S_y is multiplied by a uniform loss factor of $e^{-\gamma} = 0.9$.

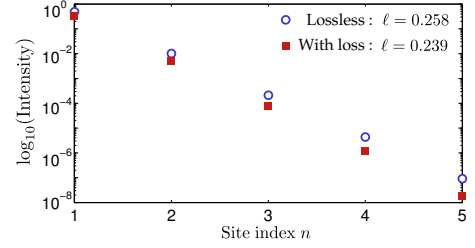


FIG. 9. Semilog plot of the edge state intensity versus ring index n , for lossless (blue circles) and lossy (red squares) networks respectively. The network consists of an infinite strip 5 unit cells wide, with line delay $\phi = 0.2\pi$ and coupler strength $\theta = 0.4\pi$ (which matches the “strong coupling” regime of the experiment). For the lossy system, we add loss $e^{-\gamma}$ to each quarter-ring segment, where $\gamma = 0.25$. For both cases, the edge state at $k = -0.4\pi$ is shown. The intensity at each unit cell is defined as the sum of the absolute squares of the wave amplitudes on the four quarter-ring segments (cf. Fig. 6).

in the complex plane, as k is wound through 2π , for a lossy network. Here, we have taken a uniform factor $\exp(-\gamma_\mu^{ij}) = 0.9$ in all couplers. It can be seen that the behavior is similar to our experimental results (Fig. 3 of the main text). In particular, deep in the topologically trivial or non-trivial phase ($\theta = 0.1\pi$ and $\theta = 0.4\pi$ respectively), the eigenvalue trajectories are clearly continuable to the zero-winding and nonzero-winding behavior of the lossless system.

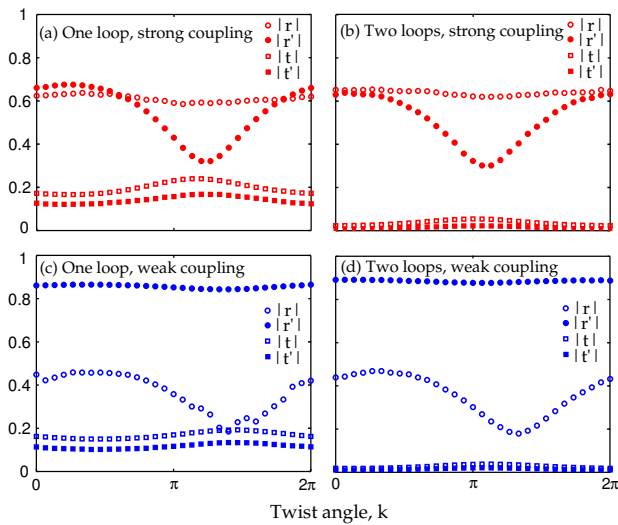


FIG. 10. Experimentally-measured reflection coefficient magnitudes ($|r|$ and $|r'|$, circle symbols) and transmission coefficient magnitudes ($|t|$ and $|t'|$, square symbols), versus phase shift k . Results are shown for the strong and weak coupling regimes, and for the one-loop and two-loop configurations. Unprimed and primed coefficients refer to waves incident on the left and right edges, respectively. In the two-loop configurations, the transmission becomes negligible.

Appendix C: Insulation and edge state localization

Strictly speaking, topologically nontrivial behavior emerges in a sample only in the limit where opposite edges are spatially well-separated. In terms of the topological edge states, the wavefunctions for edge states on opposite edges must have negligible overlap.

In order to determine the penetration depth of the edge states, we consider a hypothetical strip with an ample width of 5 unit cells in the \hat{x} direction (and infinite in the

\hat{y} direction). Fig. 9 shows the semilog plot of the intensity (defined as the absolute square of the wave amplitudes in the links) versus distance along the \hat{x} direction (measured in lattice units), for a typical mid-gap edge state. Two distinct cases are considered: with loss levels similar to those in the experiment, and without loss. All other network parameters, including the coupling constant θ , are chosen to be similar to the topologically nontrivial regime of the actual experiment.

From this plot, we see that the edge states in both the lossless and lossy networks are exponentially localized to one edge: the intensity scales as $I_n \propto \exp(-n/\ell)$, where n is the site index in the \hat{x} direction. A numerical fit gives a penetration depth of $\ell \approx 0.258$ unit cells for the lossless network. Introducing losses decreases this only slightly, to $\ell \approx 0.239$ unit cells. Hence, we can conclude that the edge states have negligible overlap even for a network two unit cells wide, as in the experiment. Furthermore, the penetration depth is mainly determined by the bandgap, not by the losses in the network.

We can also verify that the edges are spatially well-separated by using direct experimental data. In the scattering formulation of the topological pump (described in Section II.B of the main text), the edges are well-separated if waves incident on one edge of the cylindrical sample have negligible transmission to the opposite edge [21]. Fig. 10 shows reflection and transmission coefficients measured by the network analyzer in the experiment. For both strong and weak couplings, the transmission decreases significantly when going from the single-loop configuration (corresponding to a one cell wide cylinder) to the two-loop configuration (corresponding to a two cell wide cylinder). For the latter, the magnitude of the transmission coefficient is less than 0.06 (for strong coupling) and less than 0.04 (for weak coupling). Thus, this line of reasoning likewise indicates that we are justified in interpreting the behavior of the two-loop network in terms of topological insulator physics.

-
- [1] M. Stone, *Quantum Hall Effect* (World Scientific, 1992).
 - [2] J. E. Moore, *Nature* **464**, 194 (2010).
 - [3] F. D. M. Haldane and S. Raghu, *Phys. Rev. Lett.* **100**, 013904 (2008).
 - [4] S. Raghu and F. D. M. Haldane, *Phys. Rev. A* **78**, 033834 (2008).
 - [5] Z. Wang, Y. D. Chong, J. D. Joannopoulos, and M. Soljačić, *Phys. Rev. Lett.* **100**, 013905 (2008).
 - [6] Z. Wang, Y. D. Chong, J. D. Joannopoulos, and M. Soljačić, *Nature* **461**, 772 (2009).
 - [7] W.-J. Chen, S.-J. Jiang, X.-D. Chen, J.-W. Dong, and C. T. Chan, *arXiv:1401.0367*.
 - [8] M. C. Rechtsman, J. M. Zeuner, Y. Plotnik, Y. Lumer, D. Podolsky, F. Dreisow, S. Nolte, M. Segev, and A. Szameit, *Nature* **496**, 196 (2013).
 - [9] M. Hafezi, E. A. Demler, M. D. Lukin, and J. M. Taylor, *Nature Phys.* **7**, 907 (2011).
 - [10] M. Hafezi, S. Mittal, J. Fan, A. Migdall, and J. M. Taylor, *Nat. Photonics* **7**, 1001 (2013).
 - [11] K. Fang, Z. Yu, and S. Fan, *Nature Phot.* **6**, 782 (2012).
 - [12] J. Koch, A. A. Houck, K. Le Hur, and S. M. Girvin, *Phys. Rev. A* **82**, 043811 (2010).
 - [13] A. Petrescu, A. A. Houck, and K. Le Hur, *Phys. Rev. A* **86**, 053804 (2012).
 - [14] A. B. Khanikaev, S. H. Mousavi, W.-K. Tse, M. Kargarian, A. H. MacDonald, and G. Shvets, *Nature Materials* **12**, 233 (2013).
 - [15] Y. Lumer, Y. Plotnik, M. C. Rechtsman, and M. Segev, *Phys. Rev. Lett.* **111**, 243905 (2013).
 - [16] K. v. Klitzing, G. Dorda, and M. Pepper, *Phys. Rev. Lett.* **45**, 494 (1980).
 - [17] D. J. Thouless, M. Kohmoto, M. P. Nightingale, and M. den Nijs, *Phys. Rev. Lett.* **49**, 405 (1982).
 - [18] R. B. Laughlin, *Phys. Rev. B* **23**, 5632 (1981).
 - [19] B. I. Halperin, *Phys. Rev. B* **25**, 2185 (1982).
 - [20] P. W. Brouwer, *Phys. Rev. B* **58**, R10135 (1998).

- [21] D. Meidan, T. Micklitz, and P. W. Brouwer, *Phys. Rev. B* **84**, 195410 (2011).
- [22] I. C. Fulga, F. Hassler, and A. R. Akhmerov, *Phys. Rev. B* **85**, 165409 (2012).
- [23] M. Pasek and Y. D. Chong, *Phys. Rev. B* **89**, 075113 (2014).
- [24] Y. E. Kraus, Y. Lahini, Z. Ringel, M. Verbin, and O. Zilberberg, *Phys. Rev. Lett.* **109**, 106402 (2012).
- [25] M. Verbin, O. Zilberberg, Y. Lahini, Y. E. Kraus, and Y. Silberberg, arXiv:1403.7124.
- [26] M. Hafezi, *Phys. Rev. Lett.* **112**, 210405 (2014).
- [27] T. Oka and H. Aoki, *Phys. Rev. B* **79**, 081406 (2009).
- [28] J. I. Inoue and A. Tanaka, *Phys. Rev. Lett.* **105**, 017401 (2010).
- [29] T. Kitagawa, M. S. Rudner, E. Berg, and E. Demler, *Phys. Rev. A* **82**, 033429 (2010).
- [30] T. Kitagawa, E. Berg, M. Rudner, and E. Demler, *Phys. Rev. B* **82**, 235114 (2010).
- [31] N. H. Lindner, G. Refael and V. Galitski, *Nature Physics* **7**, 490-495 (2011).
- [32] Z. Gu, H. A. Fertig, D. P. Arovas, and A. Auerbach, *Phys. Rev. Lett.* **107**, 216601 (2011).
- [33] M. S. Rudner, N. H. Lindner, E. Berg, and M. Levin, *Phys. Rev. X* **3**, 031005 (2013).
- [34] J. T. Chalker, and P. D. Coddington, *J. Phys. C* **21**, 2665 (1988).
- [35] B. Kramer, T. Ohtsuki, and S. Kettmann, *Phys. Rep.* **417**, 211 (2005).
- [36] S. Ryu, C. Mudry, H. Obuse, and A. Furusaki, *New J. Phys.* **12**, 065005 (2010).
- [37] G. Q. Liang and Y. D. Chong, *Phys. Rev. Lett.* **110**, 203904 (2013).
- [38] G. Q. Liang and Y. D. Chong, *Int. J. Mod. Phys. B* **28**, 1441007 (2014).
- [39] T. Ozawa and I. Carusotto, *Phys. Rev. Lett.* **112**, 133902 (2014).
- [40] C. -E. Bardyn, S. D. Huber, and O. Zilberberg, arXiv:1312.6894 (2013).
- [41] J. Zeuner, M. C. Rechtsman, Y. Plotnik, Y. Lumer, M. S. Rudner, M. Segev, A. Szameit, arXiv:1408.2191 (2014).